

Revisiting the depth distribution of seismicity before and after the 2004–2008 eruption of Mount St. Helens



Han Zhang ^{a,*}, Margaret Glasgow ^a, Brandon Schmandt ^a, Weston A. Thelen ^b, Seth C. Moran ^b, Amanda M. Thomas ^c

^a Department of Earth and Planetary Sciences, University of New Mexico, Albuquerque, NM, USA

^b U.S. Geological Survey, Cascades Volcano Observatory, Vancouver, WA, USA

^c Department of Earth Sciences, University of Oregon, Eugene, OR, USA

ARTICLE INFO

Keywords:

Mount St. Helens
Seismicity
Hypocenter
Long-term catalog

ABSTRACT

Hypocenter estimation at active volcanoes improves our understanding of their magmatic systems and indicates changing conditions at depth for continuously monitored volcanoes. The most active volcano in the Cascades Range, Mount St. Helens, has a multi-decadal earthquake catalog and it shows an apparent change in the depth distribution of seismicity before and after the 2004–2008 dome-building eruption and unrest sequence. We use two new resources to evaluate the accuracy of hypocenters and consequently the change in depth distribution of seismicity before and after the 2004–2008 eruption. First, we deployed a dense array of 136 three-component nodal seismographs for one month in 2017, including sub-arrays on the newly extruded dome and crater floor. Second, for events recorded during this month, we located their hypocenters using a three-dimensional (3D) waveform-tracking location solver and a recently developed tomography model derived from active and passive source data. The relocated hypocenters are generally shallower and more concentrated beneath the crater compared to their catalog locations. The mean hypocenter movement from catalog locations is 2.86 km, with an averaged depth shift of 2.53 km upward. Comparison between 2017 hypocenters located using all of the available phase picks and those located using only the catalog picks from the permanent network suggests the improved hypocenters mostly resulted from the location solver and the 3D velocity model, with smaller changes due to the dense three-component array. Applying the same hypocenter estimation method to phase picks for all events from 1997 to 2004 and 2008–2021, we found a concentration of seismicity between sea level and ~1 km above it before and after the 2004–2008 eruption. The new results suggest that the seismogenic structure in the shallow magmatic system quickly re-equilibrated to its earlier state after the dome-building eruption.

1. Introduction

Seismicity is an important indicator of changes in the magmatic system at depth beneath active volcanoes (Pesicek et al., 2018). Changes in the rate, locations, and source types can provide insight into changing conditions in the magmatic system. For example, Shapiro et al. (2017) identified earthquake clusters at two distinct depths near the Klyuchevskoy volcano group and proposed a fluid pressure transfer between the deep source and the shallow magma system preceding volcano eruptions. Cesca et al. (2020) observed fast upward migration of the seismicity from the Moho to the surface near Comoros island and interpreted it as the drainage of a deep magma reservoir. Roman and Cashman (2018) analyzed earthquake catalogs preceding six well-

monitored volcanic eruptions and proposed a top-down model for long multi-stage precursory sequences. The reliability of these interpretations and their ability to inform future hazard forecasting heavily depends on the accuracy of earthquake detection and hypocenter estimation, especially estimates of focal depths.

Mount St. Helens is the most active volcano in the Cascades Range and has been monitored for more than four decades (Dzurisin, 2018). The permanent seismic stations operated by the Pacific Northwest Seismic Network (PNSN) and USGS Cascades Volcano Observatory routinely detect and locate local earthquakes (<https://pnsn.org/>). The decades-long catalog contains precursors to the 2004–2008 dome-building eruption and has been advancing our understanding of the evolution of the magma system from the 1980 eruption to the present

* Corresponding author.

E-mail address: hanzhang@unm.edu (H. Zhang).

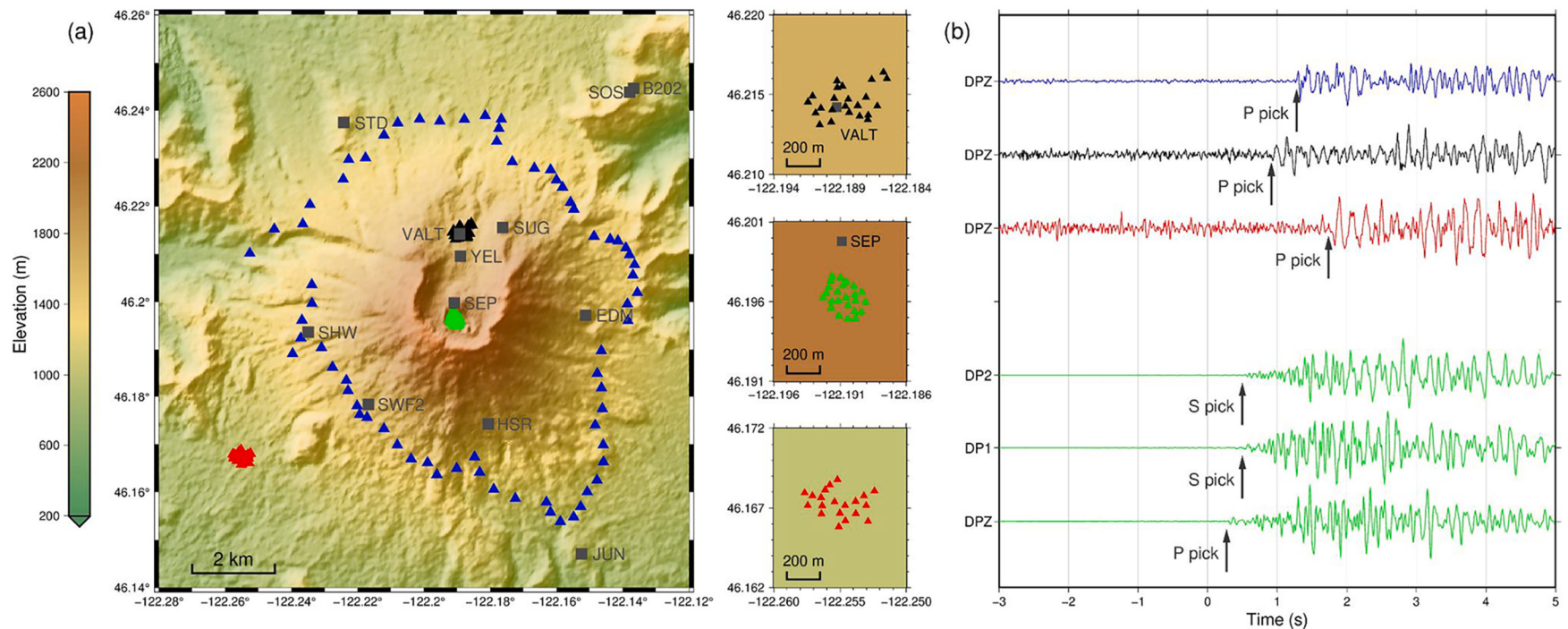


Fig. 1. Map of seismic stations and phase pick examples. (a) The node stations are represented by colored triangles based on their locations and the side panels show detailed layout of the three densely spaced sub-arrays. The permanent stations are denoted by gray squares labeled with their names. (b) The waveform examples are color coded using the same strategy as in the station map. The node channel names are shown along the traces. The DP1 records the north-south motions, DP2 records east-west motions, and DPZ records vertical motions.

Table 1

The permanent stations used in this study.

Network	Station	Operation	Channel
CC	STD	2004-10-05	3C
CC	SEP	2004-11-05	Z/3C*
CC	VALT	2006-09-30	3C
CC	SUG	2009-08-07	Z/3C*
CC	SWF2	2013-08-29	3C
UW	SHW	1972-10-01	Z/3C*
UW	SOS	1980-05-16	Z
UW	EDM	1980-06-01	Z/3C*
UW	HSR	1985-08-12	Z
PB	B202	2007-07-05	3C
UW	JUN	1980-05-08 to 2019-07-12	Z
UW	YEL	1981-10-01 to 2007-09-18	Z
UW	STD	1982-05-01 to 2017-09-14	Z
UW	SEP	1997-09-01 to 2004-10-06	Z

Note: Operation only includes the start date if the station is still working. Z in the channel column means vertical component seismometers and 3C means 3-components seismometers. Vertical component stations that were upgraded to 3C are indicated (*). The CC-SEP was upgraded to 3C on 2013-04-30. The CC-SUG was upgraded to 3C on 2014-07-29. The UW-SHW and UW-EDM were upgraded to 3C on 2021-06-18.

(Moran et al., 2008; Thelen et al., 2008). The catalog is widely cited to infer the depths of magma reservoirs (e.g. Blundy et al., 2008), to identify temporal pressure changes at depths (e.g. Moran, 1994; Musumeci et al., 2002; Lehto et al., 2010; Lehto et al., 2013), and to construct regional seismic tomography models (e.g. Lees and Crosson, 1989; Waite and Moran, 2009; De Siena et al., 2014; Kiser et al., 2016; Kiser et al., 2018; Ulberg et al., 2020). To increase the reliability of their products, these studies often require empirical constraints such as a minimum azimuth gap, distance to nearest station (delta) and/or a travel time residual threshold to discard less constrained hypocenters. However, when focusing on tracking spatiotemporal changes in the magmatic system, using the catalog hypocenters may suffer from systematic bias introduced by changing network geometry and inversion methods over time. There is an apparent change in the depth distributions before and after the 2004–2008 eruption in the PNSN catalog. Given the network densification and instrument upgrades during the 2004–2008 dome-building eruption, the improved subsurface velocity profile from a densely placed temporary array in 2005 (Thelen et al., 2008), and

changes in PNSN's processing system as well as location methods in 2011, a direct comparison of the catalog hypocenters may lead to misinterpreted conclusions. Instead, using a constant inversion workflow to locate the local seismicity should be preferred when inferring the spatiotemporal evolution of the magmatic system.

Temporary nodal seismographs (node) have been used to augment the spatial coverage of permanent stations at various environments and have shown great flexibility in their deployment (Glasgow et al., 2018; Wang et al., 2020). Such flexibility motivates examining the reliability of the local catalog at Mount St. Helens and can separately investigate the contributions from an improved array geometry and an improved location approach. In this work, we used the data from a dense nodal array at Mount St. Helens in the summer of 2017 to relocate catalog events and evaluate the accuracy of their hypocenters. Motivated by the differences from the existing catalog during the month of the dense array, we then relocated events from the longer term catalog between 1997 and 2022 using PNSN phase picks that are available from the ANSS Comprehensive Earthquake Catalog (ComCat, <https://earthquake.usgs.gov/data/comcat/>). Cumulatively, the short-term and long-term relocation results provide new insights into the evolving depth distribution of seismicity at Mount St. Helens.

2. Data and methods

The temporary seismic network YI contains 136 three-component nodal seismographs that recorded continuously from 2017 to 08-19 to 2017-09-26 (39 days, all dates in this manuscript are in UTC) at a sampling rate of 250 Hz. These Magseis Fairfield Zland 3C nodes contain 5-Hz geophones and 24-bit digitizers. Based on the node locations, we divided them into four subarrays that are color coded in Fig. 1. The subarray on the southwest side (red) has 20 nodes. The 'new dome' array (green) has 24 nodes and was placed on the dome extruded during the 2004–2008 eruption. Its center is located ~500 m south from the CC-SEP station, which is located on the dome that grew over several years following the 1980 eruption (Lipman and Mullineaux, 1981; Endo et al., 1981; Weaver et al., 1981; Swanson et al., 1983; Malone et al., 1983). The crater floor array (black) has 23 nodes and was placed near the CC-VALT station. The ring array (blue) has 69 nodes and surrounds the volcano with an average radius of ~5 km. Moreover, there are 11 permanent stations in our study area during the period and they are denoted

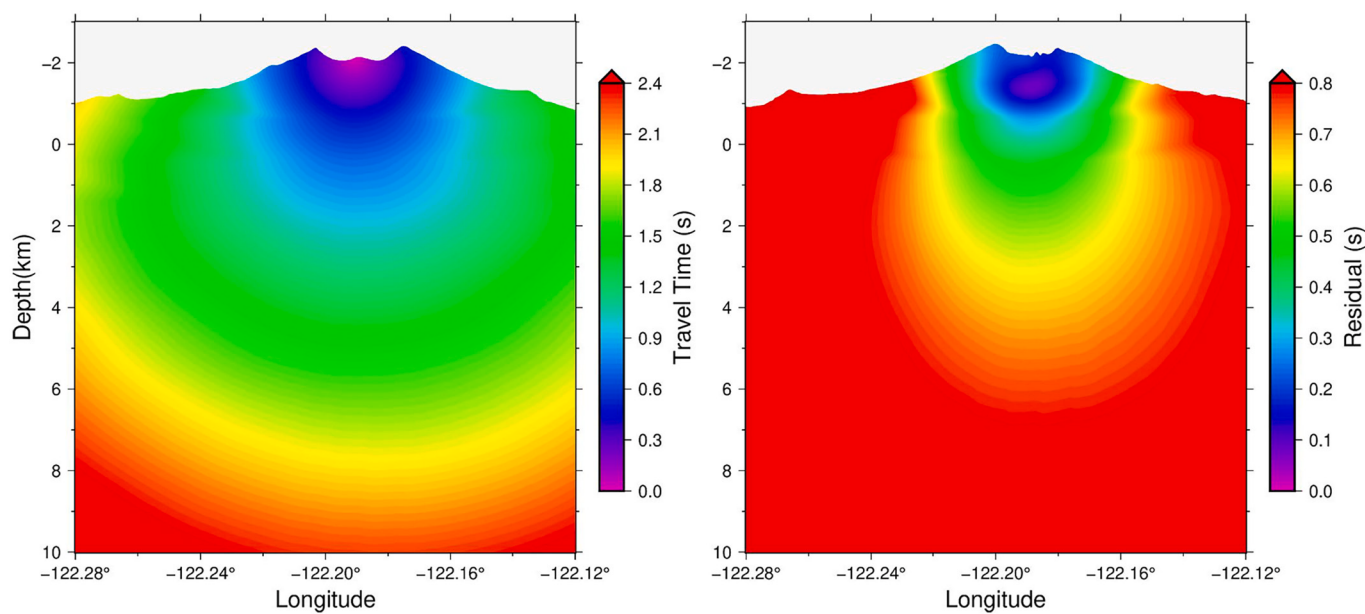


Fig. 2. Examples of three-dimensional travel time table and travel time residuals when locating the event. (Left) P wave travel time field from station SEP. (Right) a residual time example from event 2017-08-24T05:16:36.

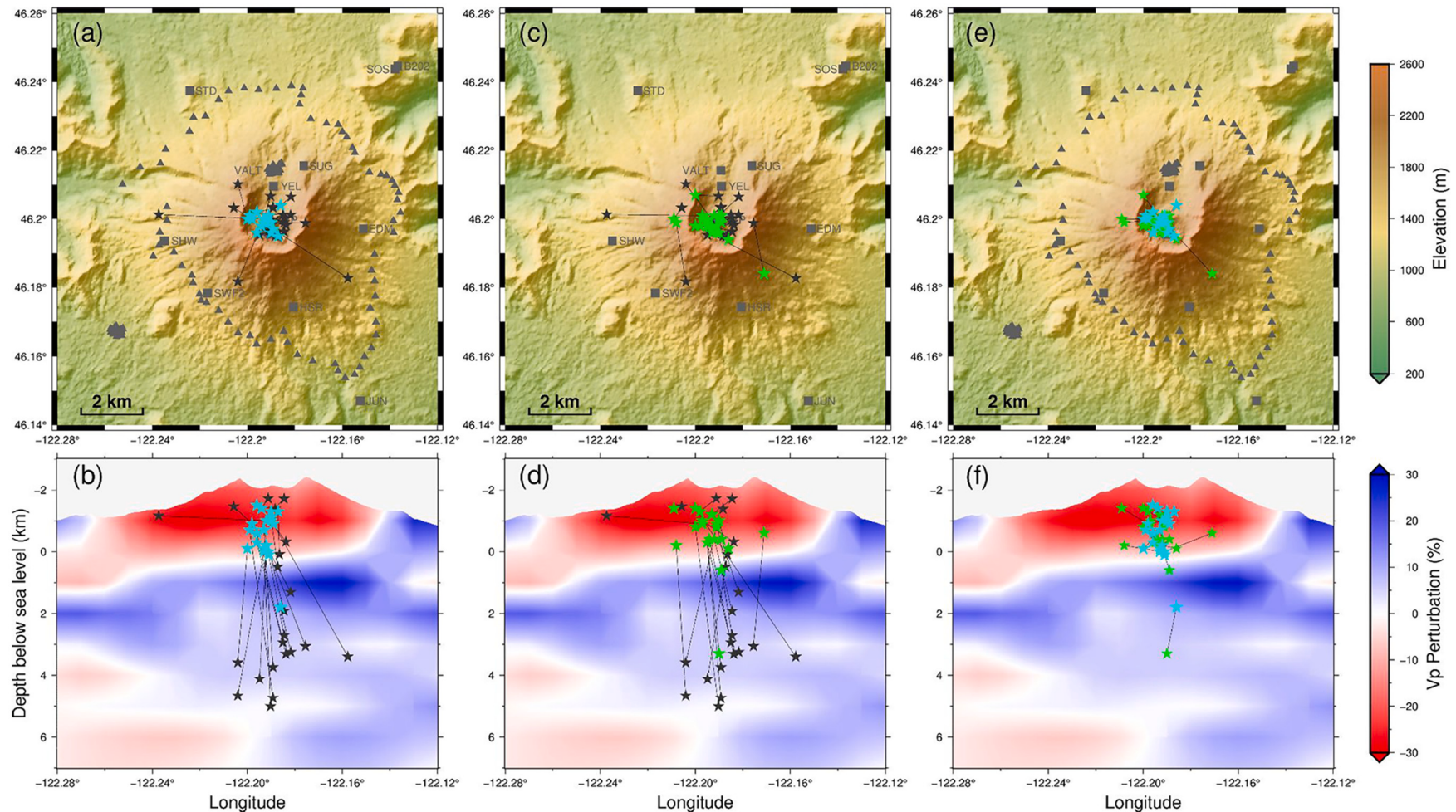


Fig. 3. Comparison of three approaches to locate seismicity during the node array. The preferred earthquake hypocenters using all phase picks from the node and Pacific Northwest Seismic Network (PNSN) arrays (cyan stars), using only PNSN picks with the hypocenter estimation method from this study (green stars), and the PNSN catalog locations (black stars) are shown. The cross-sections in (b, d, f) are sliced along a latitude of 46.20°. The Vp perturbations are taken from the tomography model of Kiser et al. (2016). (a, b) Comparison between the preferred hypocenters when using all available picks (cyan) and the PNSN catalog locations (black). (c, d) Comparison between hypocenters estimated using PNSN picks with the estimation method from this study (green) and their PNSN catalog locations (black). (e, f) Comparison between the preferred hypocenters when using all picks (cyan) with those estimated using only PNSN picks (green) but with the same hypocenter estimation method from this study. (For interpretation of the references to color in this figure legend, the reader is referred to the web version of this article.)

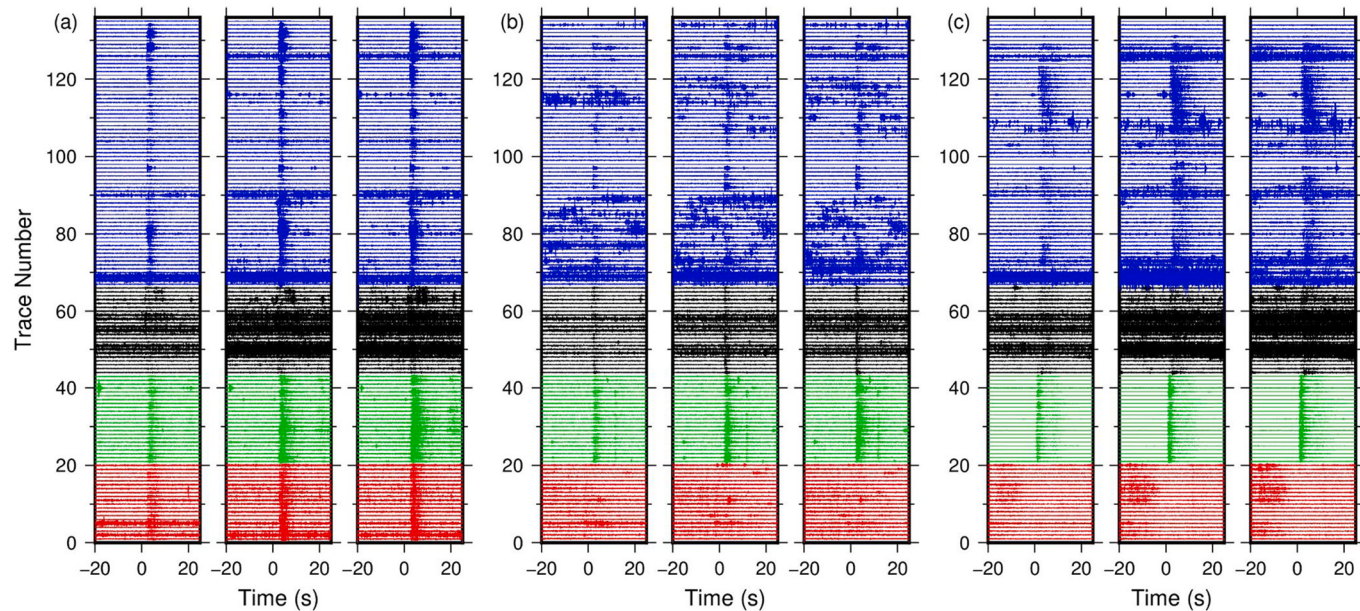


Fig. 4. Waveform examples from events with three different depths. The waveforms are color-coded to match the station locations in Fig. 1. (a) event depth of 1.8 km below sea level. The three columns show the DPZ (vertical), DP1 (north-south), and DP2 (east-west) channels from the left to right respectively. (b) same as (a) but for an event depth at sea level (0.0 km). (c) same as (a) but for an event depth of 1.4 km above sea level (-1.4 km).

by gray squares in Fig. 1 and their channel information and operation periods can be found in Table 1.

During the node deployment, the PNSN catalog reported 24 events within 5 km of the center of the crater (46.20° , -122.19°). The PNSN generated catalog was accessed through USGS's ComCat (<https://earthquake.usgs.gov/data/comcat/>). Their catalog magnitudes (local or duration magnitude) range from -0.2 to 1.2. These events are typical volcano-tectonic earthquakes (Chouet and Matoza, 2013) with prominent body wave arrivals. We successfully identified 23 of the 24 catalog events from the node array and made ~ 1000 phase picks (see examples from Fig. 1). We were able to pick S onsets for 15 events and most of them came from the dome array and SEP. For comparison, the events have median numbers of 6 P picks and 2 S picks for their PNSN hypocenters. Adding the node array boosts the median number of P and S picks to 36 and 2, respectively. We assigned a uniform weight (1.0) for all the picks from the permanent stations and the ring array. The southwest, dome and floor arrays were each assigned a summed weight of 2.0 for their P picks if there are more than 2 phase picks. If there is only one phase pick from the arrays, the weight is 1.0. The same weighting was used for S picks. This makes the contributions from the three dense sub-arrays twice as important as a single station but avoids overweighting them since they are too closely spaced to be considered completely independent observations.

When extending the relocated catalog to between 1997 and 2022, we avoided the time of the 2004–2008 eruption to focus on background seismicity and used the phase picks from PNSN to maintain a common set of input data. Our analysis starts in 1997 because the dome station SEP was installed in that year. The 2004–2008 eruption was avoided because of the extreme rate of seismicity and the likelihood that abundant shallow seismicity and tremor diminished the ability to detect deeper events (Moran et al., 2008). The network evolved over the study period, mostly by the addition of new stations and upgrades from a vertical component to 3-component seismographs (Table 1). The only exception in our study region is the station YEL which was removed on 2007-09-18 and replaced by VALT. The two stations are a few hundred meters apart and therefore provide similar constraints on earthquake hypocenter estimates. Thus, we included the station for events before its retirement. We requested PNSN phase picks and their associated weights from events with epicenters within 5 km from the crater's center. We

discarded events with less than 4 phase picks since we cannot reliably locate them. The choices mentioned above result in 7321 total events for relocation between 1997 and 01-01 and 2022-03-01.

To estimate hypocenters of the local events, we used a location solver that employs the fast marching method (Rawlinson and Sambridge, 2004) for three-dimensional (3D) wavefront tracking to trace P and S rays from each station to make 3D travel time tables (Fig. 2). We adopted the 3D P-wave velocity model from Kiser et al. (2016) and generated an S-wave velocity by scaling the P-wave model using the empirical relationships from Brocher (2005). Topography effects were accounted for by filling the air layer grids with a velocity of 0.34 km/s. The air layer was defined as grids above the surface topography from a 30 m digital elevation model (U.S. Geological Survey, 2017). The velocity of 0.34 km/s represents the speed of sound in air at 20°C . The grid interval along both latitude and longitude directions is 0.001° and that along the depth dimension is 0.1 km. We then calculated the hypocenters by minimizing a weighted L2 misfit between the predicted and measured arrival times (see an example in Fig. 2). Minimizing an L2 misfit will automatically require the event origin time to be the weighted average of origin time estimates from all stations. Consequently, the absolute location algorithm only searches in three dimensions.

3. Results

When relocating the 23 PNSN events that occurred during the 2017 nodal deployment, the resulting hypocenters concentrate beneath the crater at depths between sea level and 1 km above it (Fig. 3a and b). The mean hypocenter movement from catalog locations is 2.86 km with an averaged depth movement of 2.53 km upward. Locating the events with only the P picks from all stations gives similar hypocenter results (Fig. S1 and Fig. S2), suggesting that our results are not highly dependent on interpretations of S-wave onsets.

To separate the effects of adding the dense node array from the effects of the hypocenter estimation approach, the hypocenters for the same events were also estimated using only the PNSN array but with the location solver from this study using a 3D velocity model (Fig. 3c and d). The relocated hypocenters are also more concentrated beneath the crater. When comparing the two sets of relocated hypocenters, we see minor improvements from adding the node array picks in addition to the

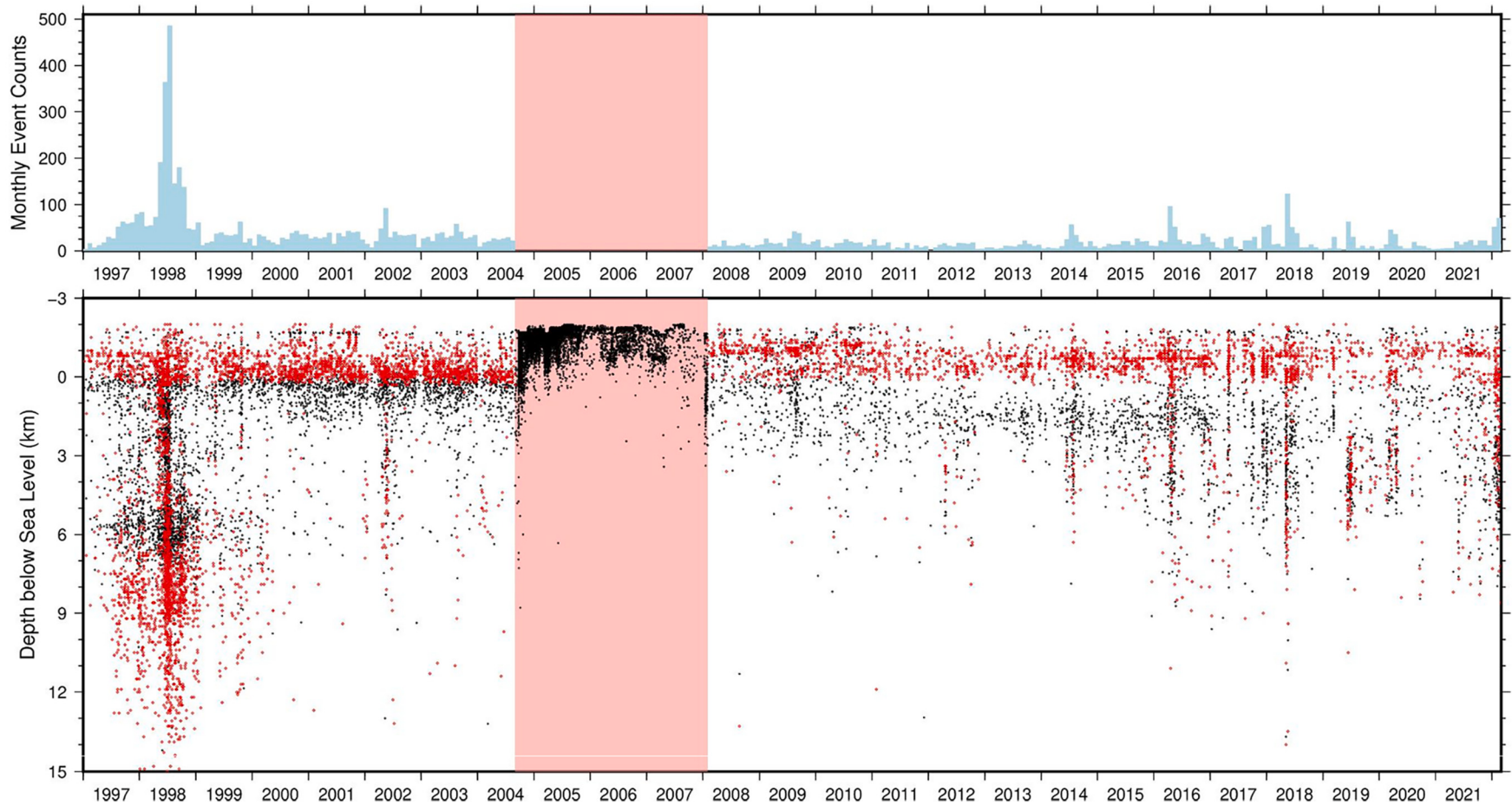


Fig. 5. Seismicity rate and depth distribution beneath Mount St. Helens from 1997 to 2022. Monthly event count is shown for events within 5 km of Mount St. Helens, with depths from our relocated catalog (red) and the Pacific Northwest Seismic Network (PNSN) catalog (black). The 2004–2008 dome-building eruption period is covered by the pink box and earthquakes from that period were not relocated. (For interpretation of the references to color in this figure legend, the reader is referred to the web version of this article.)

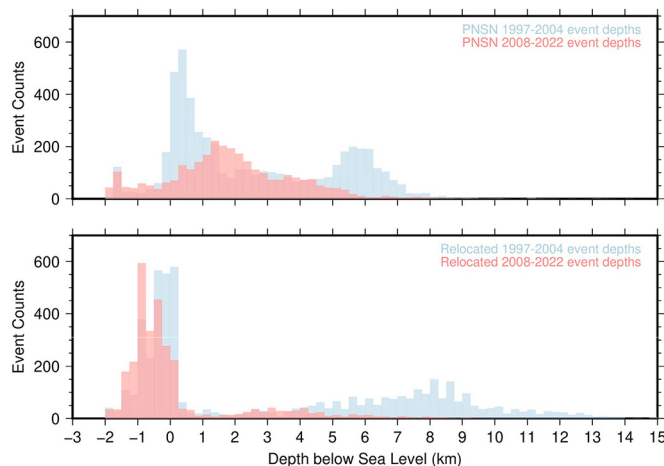


Fig. 6. Estimates of the depth distribution of Mount St. Helens seismicity. The depth distribution of pre-2004 (blue) and post-2008 (red) local events at Mount St. Helens from the Pacific Northwest Seismic Network (PNSN) catalog (top) and from the relocated catalog (bottom). (For interpretation of the references to color in this figure legend, the reader is referred to the web version of this article.)

PNSN picks (Fig. 3e and f). A tighter horizontal clustering of seismicity beneath the dome complex in the summit crater is shown with the dense node array. The mean hypocenter movement is 0.73 km with an average depth movement of 0.37 km. These movements are much smaller than those from the PNSN locations to our preferred results, which are 2.86 km for hypocenter and 2.53 km for depth. We also used Hypoinverse (Klein, 1985), which is the one-dimensional (1D) location algorithm used at PNSN, to locate these events with all available phase picks. The relocated event depths are similar to those in the catalog (Fig. S3). These comparisons suggest that the 3D velocity model and the ray tracing algorithm play more important roles in updating the hypocenters. Assuming the 3D velocity models can be used for locating earlier seismicity at Mount St. Helens, our finding motivates relocation of the longer-term catalog to check for potential systematic bias.

Node waveform examples from three different depths provide further indications that most seismicity is shallow and centrally located beneath the dome array. We show the waveforms from example events with depths of 1.8, 0, and -1.4 km below sea level, respectively (Fig. 4). The traces are color-coded to match their locations in Fig. 1 and are sorted by azimuth within each sub-array. We see that only the deep event clearly excites signals on the southwest array, which is farther from the dome (Fig. 4a). In contrast, the sea level event lacks clear expression on the southwest array (Fig. 4b). The shallowest event only generates clear signals at the dome stations and some ring stations, which have long coda on their horizontal components possibly due to reverberation within the edifice (Neuberg and Pointer, 2000). Moreover, the arrival times at the ring stations become later than those from the dome array for the shallowest event (Fig. 4c), which is consistent with a shallow origin.

We extended the relocated catalog to local events at Mount St. Helens from 1997 to 2022 (Fig. 5). We excluded the events during the 2004–2008 dome-building eruption due to our focus on background seismicity at Mount St. Helens. After discarding events with a relocated epicenter more than 5 km from Mount St. Helens, the preferred earthquake depths form a continuous band of seismicity between sea level and ~1 km above it (Fig. 5, see Fig. S4 for a version without event depths from PNSN). For the cumulative study period, about 66% (4866 out of 7321) of the relocated events move to a shallower depth with an average upward movement of 1.68 km. Focusing on the post-2008 events, about 86% move to a shallower depth with an average upward movement of 2.16 km. The concentration of seismicity between sea level

and ~1 km above it still exists even if we locate the post-2008 events using only the stations available before 2004 (Fig. S5 and Fig. S6), suggesting that array geometry plays a minor role in the depth estimates.

4. Discussion

The most prominent result of the earthquake relocation analysis is that the depth distribution of seismicity at Mount St. Helens post-2008 is more similar to the depth distribution prior to the 2004–2008 dome-building eruption (Fig. 6). The PNSN catalog shows a concentration of seismicity between -1 to 0 km below sea level prior to 2004 but that is replaced by deeper and more diffuse events between 0 and 3 km below sea level following the 2004–2008 eruption, apparently indicating a change in seismogenic structures within the Mount St. Helens magmatic system. The distinct depth distributions were taken as evidence of a slower pressurization rate of the shallow conduits beneath Mount St. Helens after the 2004–2008 dome-building eruption (Dzurisin, 2018). However, the relocated catalog eliminates the basis for such an interpretation of change in the magmatic system (Fig. 6). The relocated results using a consistent velocity model and processing approach for the entire study period show that concentrated seismicity at -1 to 0 km below sea level persists before and after the 2004–2008 dome-building (Fig. 6). Subtle pre- and post-eruption changes are observed in the relocated catalog, such as a greater concentration of events near -1.5 km below sea level from 2008 to 2010, which suggests a slight shallowing of seismicity rather than a deepening in previous results (Fig. 5). However, the dramatic change between the pre- and post-eruption depth distribution in the PNSN catalog becomes much more subdued in the relocated catalog (Fig. 6). The main change that remains in the relocated catalog is that the number of events at depths greater than 5 km below sea level is greater prior to 2004, which mostly results from an elevated rate of deeper seismicity and inferred magmatic recharge centered in 1998 (Musumeci et al., 2002; Fig. 5).

Since the PNSN catalog and our new long-term relocation results used the same phase picks, the difference is most likely due to the difference in locating methods. The location algorithm used by PNSN (Hypoinverse) traces P and S rays in a 1D velocity model and introduces empirical station corrections to account for 3D velocity anomalies and site topography. Consequently, inconsistent empirical corrections from different stations could lead to systematic location bias that can change each time a station is added or removed. Several stations were added or upgraded during the 2004–2008 eruption (Table 1 and Fig. S6), thereby providing one potential source of bias when comparing pre-2004 and post-2008 hypocenters. Alternatively, the difference in the location solver could introduce bias in the results. In 2011, PNSN switched from SPONG, an adaption of FASTHYPO (Herrmann, 1979) to Hypoinverse (Klein, 1985). Subtle differences in inversion techniques between the two methods can lead to differences in locations, where a local minimum may be preferred erroneously. This behavior has been recognized anecdotally for some events at Mount St. Helens, though never published. In contrast, here we fixed the 3D velocity model, location method and ray tracing method for both periods, making the relocated hypocenters more comparable. Additionally, we tested the effects of using only the stations available before 2004 and found a similar event depth distribution (Fig. S5). Therefore, we suggest that the relocated time-depth results better represent the distribution of seismicity beneath Mount St. Helens before and after the 2004–2008 eruption.

Most of the relocated event depths are between sea level and ~1 km above it (Fig. 6), which is significantly shallower than petrologic studies suggest for the localized sources of magma that fed the 2004–2008 dome-building eruption (~3 km beneath sea level from Pallister et al., 2008). The concentration of shallow seismicity is also shallower than the estimated depths of the primary upper crust magma chamber at Mount St. Helens: ~5–11 km below sea level from Blundy et al. (2008); 3.5–14 km below sea level from Kiser et al. (2018); 3–12 km beneath surface from Hill et al. (2009); and a top depth of 3–8 km beneath surface from

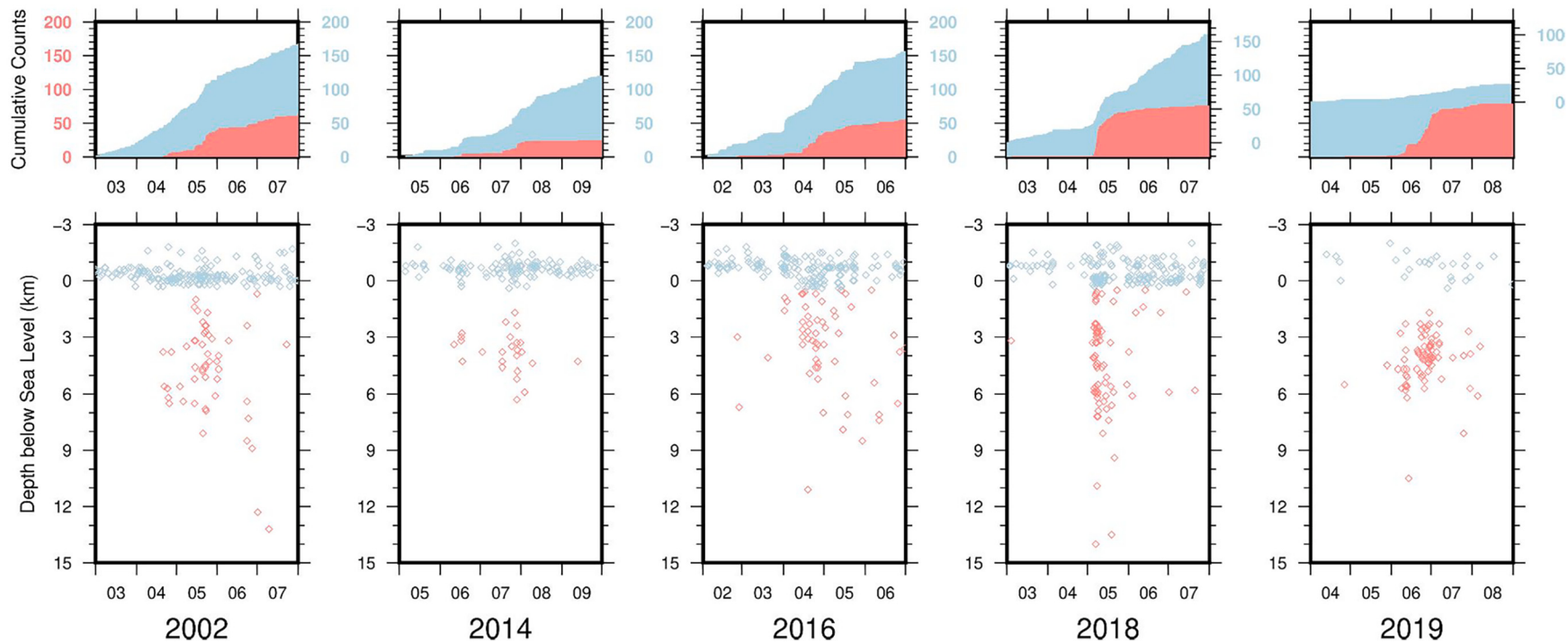


Fig. 7. Comparison of shallower and deeper activity during episodes of elevated seismicity. (Top) The cumulative event counts of shallow (blue; less than 0.5 km below sea level) and deep (red; greater than 0.5 km below sea level) earthquakes during a five-month window. A flat line means no earthquakes and increases in slope represent increases of seismicity rate. Note that the deep events (red, left side) share a vertical axis but the vertical axis of shallow earthquakes (blue, right side) counts in 2018 and 2019 are different from the other 3 panels. (Bottom) The time-depth distribution of the seismicity. The horizontal axis marks the year and the months. (For interpretation of the references to color in this figure legend, the reader is referred to the web version of this article.)

[Anderson and Segall \(2013\)](#). Consequently, the isolated shallow peak in seismicity may represent stress rebalance in conduits above magma storage depths, perhaps as a result of magmatic volatiles migrating through fractures rather than their previous interpretation as inputs to the silicate melt reservoirs at greater depths ([Lehto et al., 2013](#)). Moran et al., (2008) proposed that the concentration of shallow seismicity before 2004 could represent a fracture zone near the base of a solid plug which extends from the surface down to sea level. If so, the continuity of shallow seismicity after the 2004–2008 eruption suggests relatively quick formation of a solid plug creating conditions similar to those of the pre-2004 period. Indeed, seismicity right at the end of the 2004–2008 eruption extended to 3 km below sea level for the first time since before the 2004 eruption ([Dzurisin et al., 2015](#)). The earthquake frequency from 2008 to 2013 (3.1 events/week) is less than half of that from 1999 to 2004 (7.0 events/week) ([Fig. 5](#)). Assuming the earthquake detection threshold is the same for the two periods, a smaller seismicity rate could represent a relatively weak solid plug or less intense pressure influx of magmatic volatiles from below.

The relocated time-depth catalog shows a strong correlation between earthquake count peaks and deep seismicity clusters ([Fig. 5](#)). The monthly count peaks in the years of 2002, 2014, 2016, 2018, and 2019 all associate with increases in volcano-tectonic seismicity ~1–10 km below sea level. To explore the temporal relationships between the shallow and deep seismicity near these peaks in detail, we calculated their cumulative event count within a five-month time window ([Fig. 7](#)). The depth to split shallow and deep events is set at 0.5 km below sea level, as suggested by the event distribution in [Fig. 6](#). The detailed view suggests various temporal patterns between earthquakes at different depths ([Fig. 7](#)). In 2002, 2014, and 2018, both the shallow and the deep seismicity show sharp increases at similar times. However, the shallow seismicity rate increases ~2 weeks before deeper seismicity in 2016. Near the seismicity elevation in 2019, the shallow seismicity appears decoupled from the deeper earthquakes. Moreover, if we look at the shallow seismicity rate before and after clustered deep earthquakes, the seismicity in 2018 also differs from that in 2014. In 2014, the elevated shallow seismicity rate decays weeks after cessation of the deeper earthquakes. In contrast, in 2018, the shallow seismicity rate stays high after the cessation of deeper earthquakes. These results suggest a complex stress transfer system beneath Mount St. Helens, in which some sequences of elevated seismicity reflect tightly coupled changes between shallower and deeper parts of the magmatic system while others involve substantial lag times.

5. Conclusions

We relocated 23 earthquakes near Mount St. Helens in 2017 with a dense array of three-component nodal seismographs and found most of the events moved to shallower depths and were more centrally focused beneath the crater. The average hypocenter movement from the Pacific Northwest Seismic Network (PNSN) catalog locations to our relocated hypocenters is 2.86 km, which is sufficiently far to confound interpretations of change in the magmatic system at depth. After comparing the hypocenter estimates from all available phase picks and from catalog phase picks, we found that most of the hypocenter movement resulted from the location method (including the input velocity model), with more minor effects due to the change in the number and spatial distribution of seismometers. The relocated hypocenters motivated longer term examination of changes in the depth distribution of Mount St. Helens seismicity. We then relocated the PNSN catalog events from 1997 to 2022 (excluding the 2004–2008 dome-building eruption) using the same phase picks but with the updated velocity model and three-dimensional location solver applied to the node array in 2017. The relocated hypocenters show a continuously active concentration of seismicity between sea level and ~1 km above it, suggesting similar magmatic conditions before and after the 2004–2008 dome-build eruption. Importantly, this result contrasts with the apparent change

in depth between the pre- and post-eruption seismicity in the PNSN catalog. Changes in the hypocenter estimation workflow, such as altered network geometry and inversion algorithm, rather than changes in the magmatic system are likely to be the origin of the apparent change in seismicity depth distribution. Thus, the relocation results highlight the importance of testing the effects of any processing changes when maintaining long-term seismicity catalogs, and they indicate that the dome-building eruption at Mount St. Helens did not cause a major long-lived reorganization of seismogenic structures near the top of its magmatic system.

Correlations between seismicity in the shallow cluster just above sea level and at greater depths below sea level suggest transient changes in stress transfer between shallow conduits and deeper magma reservoirs during periods of elevated seismicity. However, the catalog shows variable time lags between changes in the rate of shallower and deeper seismicity. Thus, it is unclear if these episodes of elevated seismicity are consistently initiated by either top-down or bottom-up processes.

Data availability

The waveform data from network CC ([Cascades Volcano Observatory/USGS, 2001](#)), UW ([University of Washington., 1963](#)) and PB ([Plate Boundary Observatory Borehole Seismic Network, n.d](#)) are available via IRIS Data Management Center (DMC, <https://ds.iris.edu/ds/nodes/dmc/>). The node waveform data from network YI ([Schmandt et al., 2017](#)) are available via the IRIS DMC in PH5 format (<http://service.iris.edu/ph5ws/>).

The catalog phase picks information are publicly available from the ANSS Comprehensive Earthquake Catalog (<https://earthquake.usgs.gov/data/comcat/>). Our phase picks for the events recorded by the temporary node deployment in 2017 are available at Mendeley Data (<https://data.mendeley.com/datasets/2vb6225kp5/1>).

CRediT authorship contribution statement

Han Zhang: Conceptualization, Methodology, Software, Visualization, Writing – original draft, Writing – review & editing. **Margaret Glasgow:** Investigation, Writing – review & editing. **Brandon Schmandt:** Resources, Supervision, Project administration, Funding acquisition, Writing – review & editing. **Weston A. Thelen:** Resources, Project administration, Writing – review & editing. **Seth C. Moran:** Resources, Project administration, Writing – review & editing. **Amanda M. Thomas:** Resources, Project administration, Writing – review & editing.

Declaration of Competing Interest

The authors declare that they have no known competing financial interests or personal relationships that could have appeared to influence the work reported in this paper.

Acknowledgements

Some instruments used in the study were provided by the IRIS PASSCAL Instrument Center. IRIS Data Services and the IRIS PASSCAL Instrument Center are funded through the Seismological Facilities for the Advancement of Geoscience (SAGE) Award of the National Science Foundation under Cooperative Support Agreement EAR-1851048. Accessibility of the PBO data is based on services provided by the GAGE Facility, operated by UNAVCO, Inc., with support from the National Science Foundation, the National Aeronautics and Space Administration, and the U.S. Geological Survey under NSF Cooperative Agreement EAR-1724794. This research was supported by NSF-EAR 2113315. Any use of trade, firm, or product names is for descriptive purposes only and does not imply endorsement by the U.S. Government.

Appendix A. Supplementary data

Supplementary data to this article can be found online at <https://doi.org/10.1016/j.jvolgeores.2022.107629>.

References

- Anderson, K., Segall, P., 2013. Bayesian inversion of data from effusive volcanic eruptions using physics-based models: Application to Mount St. Helens 2004–2008. *Journal of Geophysical Research: Solid Earth* 118 (5), 2017–2037.
- Blundy, J., Cashman, K.V., Berlo, K., Sherrod, D.R., Scott, W.E., Stauffer, P.H., 2008. Evolving magma storage conditions beneath Mount St. Helens inferred from chemical variations in melt inclusions from the 1980–1986 and current (2004–2006) eruptions. In: *A Volcano Rekindled: The Renewed Eruption of Mount St. Helens, 2006*, pp. 755–790.
- Brocher, T.M., 2005. Empirical relations between elastic wavespeeds and density in the Earth's crust. *Bull. Seismol. Soc. Am.* 95 (6), 2081–2092.
- Cascades Volcano Observatory/USGS, 2001. Cascade Chain Volcano Monitoring [Data set]. International Federation of Digital Seismograph Networks. <https://doi.org/10.7914/SN/CC>
- Cesca, S., Letort, J., Razafindrakoto, H.N., Heimann, S., Rivalta, E., Isken, M.P., Dahm, T., 2020. Drainage of a deep magma reservoir near Mayotte inferred from seismicity and deformation. *Nat. Geosci.* 13 (1), 87–93.
- Chouet, B.A., Matzoa, R.S., 2013. A multi-decadal view of seismic methods for detecting precursors of magma movement and eruption. *J. Volcanol. Geotherm. Res.* 252, 108–175.
- De Siena, L., Thomas, C., Waite, G.P., Moran, S.C., Klemme, S., 2014. Attenuation and scattering tomography of the deep plumbing system of Mount St. Helens. *Journal of Geophysical Research: Solid Earth* 119 (11), 8223–8238.
- Dzurisin, D., 2018. Mount St. Helens retrospective: Lessons learned since 1980 and remaining challenges. *Front. Earth Sci.* 6, 142.
- Dzurisin, D., Moran, S.C., Lisowski, M., Schilling, S.P., Anderson, K.R., Werner, C., 2015. The 2004–2008 dome-building eruption at Mount St. Helens, Washington: epilogue. *Bull. Volcanol.* 77 (10), 1–17.
- Endo, E.T., Malone, S.D., Noson, L.L., Weaver, C.S., 1981. Locations, magnitudes, and statistics of the March 20–May 18 earthquake sequence. *US Geol. Surv. Prof. Pap.* 1250, 93–107.
- Glasgow, M.E., Schmandt, B., Hansen, S.M., 2018. Upper crustal low-frequency seismicity at Mount St. Helens detected with a dense geophone array. *J. Volcanol. Geotherm. Res.* 358, 329–341.
- Herrmann, R.B., 1979. FASTHYPO—a hypocenter location program. *Earthquake Notes* 50 (2), 25–38.
- Hill, G.J., Caldwell, T.G., Heise, W., Chertkoff, D.G., Bibby, H.M., Burgess, M.K., Cas, R. A., 2009. Distribution of melt beneath Mount St. Helens and Mount Adams inferred from magnetotelluric data. *Nat. Geosci.* 2 (11), 785–789.
- Kiser, E., Palomeras, I., Levander, A., Zelt, C., Harder, S., Schmandt, B., Ulberg, C., 2016. Magma reservoirs from the upper crust to the Moho inferred from high-resolution Vp and Vs models beneath Mount St. Helens, Washington State, USA. *Geology* 44 (6), 411–414.
- Kiser, E., Levander, A., Zelt, C., Schmandt, B., Hansen, S., 2018. Focusing of melt near the top of the Mount St. Helens (USA) magma reservoir and its relationship to major volcanic eruptions. *Geology* 46 (9), 775–778.
- Klein, F.W., 1985. User's guide to HYPOINVERSE, a program for VAX and Professional 350 computers to solve for earthquake locations (no. 85–515). US Geological Survey.
- Lees, J.M., Crosson, R.S., 1989. Tomographic inversion for three-dimensional velocity structure at Mount St. Helens using earthquake data. *Journal of Geophysical Research: Solid Earth* 94 (B5), 5716–5728.
- Lehto, H.L., Roman, D.C., Moran, S.C., 2010. Temporal changes in stress preceding the 2004–2008 eruption of Mount St. Helens, Washington. *J. Volcanol. Geotherm. Res.* 198 (1–2), 129–142.
- Lehto, H.L., Roman, D.C., Moran, S.C., 2013. Source mechanisms of persistent shallow earthquakes during eruptive and non-eruptive periods between 1981 and 2011 at Mount St. Helens, Washington. *J. Volcanol. Geotherm. Res.* 256, 1–15.
- Lipman, P.W., Mullineaux, D.R., 1981. The 1980 Eruptions of Mount St. Helens, Washington. U.S. Geological Survey Professional Paper, 1250 (844 p., 1 plate).
- Malone, S.D., Boyko, C., Weaver, C.S., 1983. Seismic precursors to the Mount St. Helens eruptions in 1981 and 1982. *Science* 221 (4618), 1376–1378.
- Moran, S.C., 1994. Seismicity at Mount St. Helens, 1987–1992: Evidence for repressurization of an active magmatic system. *Journal of Geophysical Research: Solid Earth* 99 (B3), 4341–4354.
- Moran, S.C., Malone, S.D., Qamar, A.I., Thelen, W.A., Wright, A.K., Caplan-Auerbach, J., 2008. Seismicity associated with renewed dome building at Mount St. Helens, 2004–2005. US Geological Survey professional paper 1750, 27–60.
- Musumeci, C., Gresta, S., Malone, S.D., 2002. Magma system recharge of Mount St. Helens from precise relative hypocenter location of microearthquakes. *Journal of Geophysical Research: Solid Earth* 107 (B10), ESE–16.
- Neuberg, J., Pointer, T., 2000. Effects of volcano topography on seismic broad-band waveforms. *Geophys. J. Int.* 143 (1), 239–248.
- Pallister, J.S., Thornber, C.R., Cashman, K.V., Clyne, M.A., Lowers, H., Mandeville, C. W., et al., 2008. Petrology of the 2004–2006 Mount St. Helens lava dome—Implications for magmatic plumbing and eruption triggering. US Geological Survey 1750, 647–702.
- Pesicik, J.D., Wellik, J.J., Prejean, S.G., Ogburn, S.E., 2018. Prevalence of seismic rate anomalies preceding volcanic eruptions in Alaska. *Front. Earth Sci.* 6, 100.
- Plate Boundary Observatory Borehole Seismic Network. <https://www.unavco.org/data/strain-seismic/seismic-data/seismic-data.html>
- Rawlinson, N., Cambridge, M., 2004. Wave front evolution in strongly heterogeneous layered media using the fast marching method. *Geophys. J. Int.* 156 (3), 631–647.
- Roman, D.C., Cashman, K.V., 2018. Top-down precursory volcanic seismicity: implications for 'stealth' magma ascent and long-term eruption forecasting. *Front. Earth Sci.* 6, 124.
- Schmandt, B., Thomas, A., Thelen, W., 2017. Mount St. Helens 3C Node Array [Data set]. International Federation of Digital Seismograph Networks. <https://doi.org/10.7914/SN/YI2017>
- Shapiro, N.M., Drozniak, D.V., Drozniakina, S.Y., Senyukov, S.L., Gusev, A.A., Gordeev, E.I., 2017. Deep and shallow long-period volcanic seismicity linked by fluid-pressure transfer. *Nat. Geosci.* 10 (6), 442–445.
- Swanson, D.A., Casadevall, T.J., Dzurisin, D., Malone, S.D., Newhall, C.G., Weaver, C.S., 1983. Predicting eruptions at Mount St. Helens, June 1980 through December 1982. *Science* 221 (4618), 1369–1376.
- Thelen, W.A., Crosson, R.S., Creager, K.C., 2008. Absolute and relative locations of earthquakes at Mount St. Helens, Washington using continuous data: Implications for magmatic processes. In: *A Volcano Rekindled: The Renewed Eruption of Mount St. Helens, 2004–2006*, vol. 1750. US Geological Survey, Denver, Colo, pp. 71–95.
- U.S. Geological Survey, 2017. 1 Arc-second Digital Elevation Models (DEMs) - USGS National Map 3DEP Downloadable Data Collection: U.S. Geological Survey.
- Ulberg, C.W., Creager, K.C., Moran, S.C., Abers, G.A., Thelen, W.A., Levander, A., Crosson, R.S., 2020. Local source Vp and Vs tomography in the Mount St. Helens region with the IMUSH broadband array. *Geochem. Geophys. Geosyst.* 21 (3) (e2019GC008888).
- University of Washington, 1963. *Pacific Northwest Seismic Network - University of Washington* [Data set]. International Federation of Digital Seismograph Networks. <https://doi.org/10.7914/SN/UW>
- Waite, G.P., Moran, S.C., 2009. VP Structure of Mount St. Helens, Washington, USA, imaged with local earthquake tomography. *J. Volcanol. Geotherm. Res.* 182 (1–2), 113–122.
- Wang, R., Schmandt, B., Zhang, M., Glasgow, M., Kiser, E., Rysanek, S., Stairs, R., 2020. Injection-induced earthquakes on complex fault zones of the Raton Basin illuminated by machine-learning phase picker and dense nodal array. *Geophys. Res. Lett.* 47 (14) (e2020GL088168).
- Weaver, C.S., Grant, W.G., Malone, S.D., Endo, E.T., 1981. Post-May 18 seismicity; volcanic and tectonic implications. *US Geol. Surv. Prof. Pap.* 1250, 109–121.